Article

Measurement of the Convection Velocities in a Hypersonic Turbulent Boundary Layer Using Two-Point Cylindrical-Focused Laser Differential Interferometer

Ranran Huang, Tao Xue and Jie Wu *

School of Aerospace Engineering, Huazhong University of Science and Technology, Wuhan 430074, China
* Correspondence: jiewu@hust.edu.cn

Abstract: A two-point cylindrical-focused laser differential interferometer (2P-CFLDI) system and a conventional Z-type Schlieren were used to measure the hypersonic turbulent boundary layer on a flat plate at Mach number $Ma = 6$ and Reynolds number $Re = 1.08 \times 10^6$ m^{-1}. The boundary layer thickness at the measurement location and the noise radiation angle were obtained by post-processing the Schlieren image. The 2P-CFLDI data underwent cross-correlation analysis to calculate the mean convective velocities at different heights and compared with previous experimental and numerical results. The experimentally measured mean convective velocities agree with the trend of available DNS and experimental results. The mean convective velocity near the wall is significantly larger than the local mean velocity and is the main noise source region. Further filtering treatment shows that the convective velocity of the disturbed structure decreases gradually with the increase in the disturbance scale. The differences between convective velocities at different scales are significantly larger outside the boundary layer than inside the boundary layer, which is in agreement with the findings of the previous hot wire experiments. Near the wall, large-scale disturbances mainly determine the localized mean convective velocity, which are the main source of noise radiation for the hypersonic turbulent boundary layer.

Keywords: convection velocities; 2P-CFLDI; schlieren; hypersonic turbulent boundary layer

1. Introduction

A hypersonic wind tunnel is a facility that uses a Laval nozzle to simulate the high-speed flows encountered by vehicles or objects traveling at hypersonic speeds, which are defined as speeds above Mach 5 [1]. Hypersonic wind tunnels are essential for testing and developing various aerospace technologies, such as rockets, missiles, reentry vehicles, and scramjets. However, one of the challenges of using hypersonic wind tunnels is the presence of freestream disturbances, which are variations in the flow properties such as pressure, density, temperature, and velocity. Beckwith [2] reported that these disturbances can affect the aerodynamic performance and stability of the test models, as well as the accuracy and reliability of the measurements. Laufer [3] found that the freestream disturbances in a conventional hypersonic wind tunnel are mainly caused by the turbulent boundary layer that develops along the Laval nozzle wall. Schneider [4] indicated that these disturbances have a much higher amplitude than the ones in the real atmosphere, typically by 1~2 orders of magnitude. Therefore, it is important to investigate the mechanism of how the turbulent boundary layer produces such disturbances.

The turbulent boundary layer consists of organized structures that can generate noise radiation when they have a supersonic relative velocity. This phenomenon is known as eddy Mach wave radiation, and it was first proposed by Phillips [5] and Ffowcs Williams [6]. Laufer [7] experimentally demonstrated that the noise generated by eddy Mach wave radiation can be significant, especially at high Mach numbers, and it can propagate downstream of the nozzle exit. Therefore, it is important to understand the generation mechanism and

the characteristics of eddy Mach wave radiation, as well as its effects on the test models and the measurement systems. Kaimal et al. [8] indicated that one of the key parameters that determine noise generation is the convective velocity of the disturbance structures, which is the velocity at which they travel along the boundary layer.

Experimental data on convective velocities within the hypersonic turbulent boundary layer are still lacking due to the limitations of measurement techniques. Willmarth et al. [9] and Schewe [10] used surface-mounted pressure sensors to measure convective velocity disturbances on the walls of turbulent boundary layers. However, such measurements are limited to surface disturbances and difficult to extend for space measurements. Bull [11] and Klinner et al. [12] found that the spatial resolution and frequency response can be affected by the size limitations of the transducer, which in turn affects the accuracy of wall pressure fluctuation measurements. For spatial measurements in the boundary layer, hot-wire anemometers are often used [13–15]. Nevertheless, Russo [16] noted that due to the interventional measurement method, neighboring hot-wire probes inevitably generate weak shock waves and affect each other during the measurement process. Their influence on the results is difficult to assess, and they may introduce uncertainties in the estimation of the convective velocities. Moreover, Finke [17] mentioned that hot-wire anemometers are sensitive to temperature variations and require frequent calibration.

In recent years, the focused laser differential interferometer (FLDI) has been widely used in hypersonic flows due to its advantages of non-interference, high-frequency response, and fine spatial resolution [18–20]. Houpt and Leonov [21] modified the classical FLDI optical path by replacing the spherical lens with cylindrical lenses, constructing a cylindrical-focused laser differential interferometer (CFLDI) for 2D planar models. Hopkins et al. [22] further improved the optical path so that the beam can be contracted even in the direction perpendicular to the plane, resulting in a smaller thickness of the beam at the focal position and higher spatial resolution. Jewell et al. [23] added a Koester prism at the transmit side to form a two-point focused laser differential interferometer (2P-FLDI) system that can simultaneously obtain the density of the two measurement points in space. A 2P-FLDI system has been used to investigate the convection velocity of freestream disturbance in a Mach-6 shock tunnel by Gillespie et al. [24]. The results revealed an average difference of around 9% between the convection velocity of disturbances and theoretical freestream. This value is lower than the average convection velocity (about 70% of freestream velocity), which yields a difference of 30%, as predicted by Hildebrand et al. [25].

The purpose of this study is to investigate the convective velocities of different scale disturbances induced by a hypersonic turbulent boundary layer at different heights using a 2P-CFLDI system. The flow field in the measurement area was first visualized by Schlieren, and then the signals were inter-correlated by using the 2P-CFLDI system to simultaneously measure the time series of the disturbances at two adjacent points along the flow direction to finally obtain the convective velocities of the local disturbances. The raw signals were also filtered to compare the convective velocities of different scale disturbances. The experimental data are compared with the available experimental and DNS results. The ability of the 2P-CFLDI system to obtain convective velocities in the hypersonic turbulent boundary layer is verified, and the contribution of convective velocities from different scale disturbances is explored, leading to a better understanding of the causes of noise radiation from turbulent boundary layers.

2. Experimental Description

2.1. Facility and Test Condition

The investigation was conducted in the Mach 6 Ludwieg wind tunnel at Huazhong University of Science and Technology (HUST), which has an experimental section with an aperture of 0.5 m (as shown in Figure 1). The wind tunnel uses air as the working fluid and can be operated continuously for 100 ms. Since the operating time is sufficiently short, the walls of the test model maintain an ambient temperature of 300 K during the test time unless active wall heating is employed. The effective total pressure range of the wind

tunnel is 0.5~3 MPa, and the total temperature can reach up to 650 K. This experiment was conducted at a freestream Mach number of 6 and a Reynolds number of 1.08×10^7 m^{-1}. Detailed experimental conditions are presented in Table 1.

Figure 1. HUST's Φ0.5 m Mach 6 hypersonic Ludwieg wind tunnel.

Table 1. Experimental flow conditions.

Ma	Re_{unit} [m^{-1}]	p_0 [MPa]	T_0 [K]	T_{w} [K]
6	1.08×10^7	1	430	300

2.2. The Flat Plate Model

A turbulent boundary layer with a nominally zero pressure gradient was investigated using a 750 × 300 mm flat plate (as shown in Figure 2). The flat plate features a sharp leading edge with a 10° inclination, characterized by a radius smaller than 0.2 mm. The measurement location was established at the centerline of the flat plate, positioned 590 mm from the leading edge. At this specific location, a 3.2 mm through hole was crafted on the flat surface to facilitate the secure mounting of the pressure sensor. Auvity et al. [26] demonstrated that edge effects originate near the corners of the leading edge and subsequently propagate toward the centerline at an approximate Mach angle. Based on this estimation, the selected measurement position remains unaffected by edge effects. To minimize edge effects on both sides of the plate, the bottom edges have been chamfered at an angle of 45 degrees.
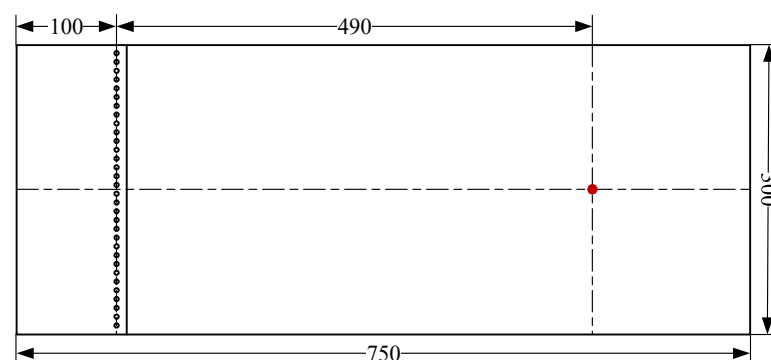

Figure 2. Geometry of flat plate and trip location (unit: mm).

Due to the constraints imposed by the current model length, a row of cylindrical tripping devices was placed 100 mm from the leading edge. The primary objective of

this arrangement was to expedite the transition process and establish a fully developed turbulent boundary layer at the designated measurement location. The three-dimensional cylindrical tripping device employed in this study is visually depicted in Figure 3. The dimensions of these tripping elements and their spatial arrangement were meticulously informed by experimental findings documented in Ref. [27]. Specifically, the tripping devices consist of a linear array of cylinders, each possessing a diameter of 3 mm and a height of 5 mm. These cylinders are uniformly spaced at 9 mm intervals along the spanwise direction.
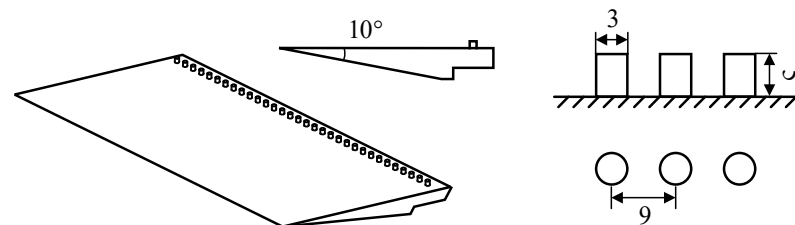

Figure 3. Geometry of boundary layer trips (unit: mm).

2.3. Measurement Methods

2.3.1. 2P-CFLDI System

In this study, a modified 2P-CFLDI system was used to quantify the statistical and structural variation of density fluctuations of the turbulent boundary layer on the flat plate. To determine convective velocities, simultaneous measurements at two adjacent points are essential. Leveraging the design principles from the 2P-FLDI [23,28–30], an additional Wollaston prism (W_0) with an increased splitting angle was introduced. This prism precedes the existing Wollaston prism (W_1) along the transmit path, effectively dividing the measurement path into two adjacent paths aligned with the flow direction. Furthermore, a right-angle reflector (R) was incorporated at the convergence point of the beam in the receive path. This arrangement ensures that the two beams propagate in opposite directions and are ultimately received by the respective detectors ($D_{1/2}$). The remaining optical elements within the optical path conform to the configuration detailed in Refs. [22,31]. For visual clarity, Figure 4 presents a schematic of the 2P-CFLDI system utilized in this experiment. Notably, the current arrangement allows for a mere 0.726 mm separation between two focal pairs at the measuring position, and only 0.0715 mm spatial resolution for per focal pair. Photograph of the setup relative to the tunnel is provided in Figure 5.
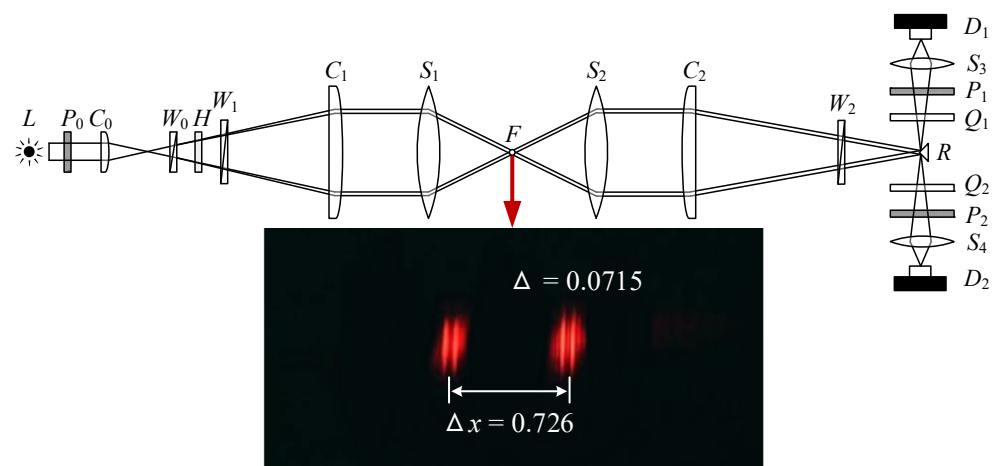

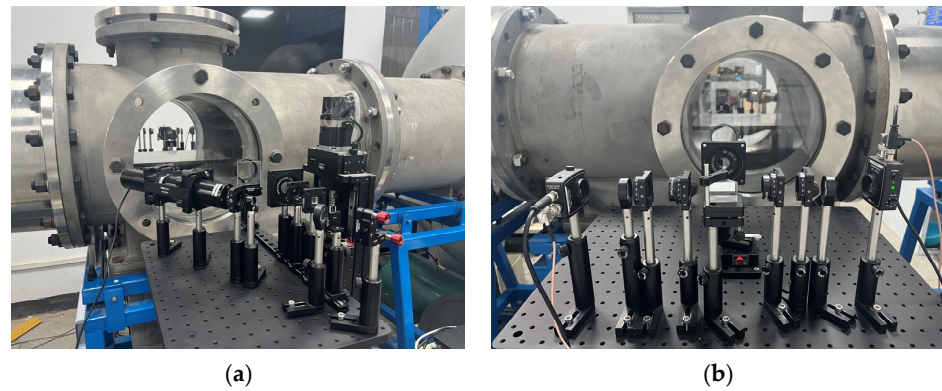**Figure 4.** Schematic of the 2P-CFLDI system and bifocal pair characterization (unit: mm).

Figure 5. Photograph of the 2P-CFLDI system setup at the HUST Ludwieg wind tunnel: (**a**) transmit side; (**b**) receive side.

Parziale's derivation provides insights into the conversion of the measured voltage signal from the FLDI system. Specifically, this conversion yields both the phase difference and the density gradient [32]. Here are the relevant equations:

$$\Delta\phi = \sin^{-1}\left(\frac{V}{V_0} - 1\right), \tag{1}$$

$$\Delta\rho = \frac{\lambda}{2\pi KL}\sin^{-1}\left(\frac{V}{V_0} - 1\right), \tag{2}$$

here, the raw measured voltage, denoted as V, corresponds to the photodetector output. The voltage with a $\pi/2$ phase shift, approximated as the average of V, is represented by V_0. The wavelength of the laser, denoted as λ, is 632.8 nm. The Gladstone–Dale constant for air, denoted as K, has a value of 2.248×10^4 m^3/kg. The integration length of the system response space is denoted as 31 mm. This length was meticulously calibrated using a CO_2 jet calibration system. Further details can be found in Ref. [31].

2.3.2. Schlieren System

A conventional Z-type parallel Schlieren technique was employed to visualize the flow density gradient (as shown in Figure 6). Illumination was provided by an HPP-120 g high-power, high-speed strobe LED light source. To manipulate the light beam, two parabolic mirrors with a diameter of 0.2 m and a focal length of 4 m were positioned. The first mirror collimated the light from the LED, ensuring parallel rays, and the second mirror refocused the collimated light toward the camera. At the refocusing position, a knife-edge cutoff was introduced to enhance the sensitivity, allowing visualization of subtle density gradients on the flat surface. An IDT NX4-S3 high-speed camera was mounted parallel to the flat surface and recorded the images. Throughout the experiments, the minimum flash time of the LED was 1 μs, and the camera sampled at a frame rate of 6000 fps.
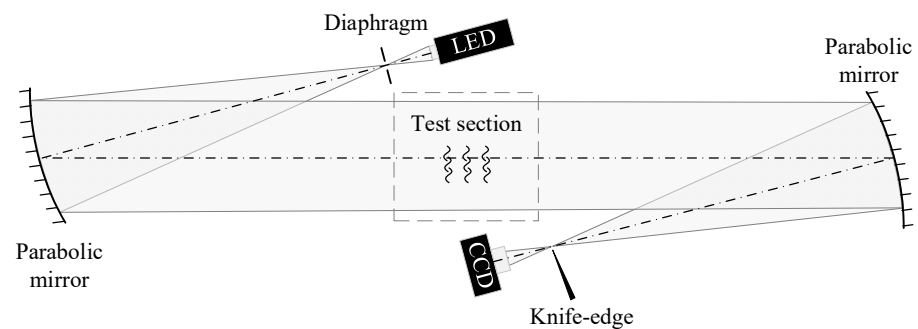

Figure 6. Schematic of the Z-type Schlieren system.

2.3.3. Piezoelectric Pressure Sensors

A PCB132B38 pressure sensor was mounted flush to the surface at the measurement location to capture wall pressure fluctuations. This sensor is specifically tailored for high-frequency pressure phenomena and excels in resolving short-wavelength, dynamic pressure pulses. The pressure sensor was calibrated for sensitivity to approximately 161.7 mV/psi before delivery. The pressure measurement resolution is no more than 1 mpsi, and the bandwidth of the effective dynamic response ranges from 11 kHz to 1 MHz.

3. 2P-CFLDI Dataset Validation

3.1. Density Gradient Fluctuations Intensity

To capture the spatial measurements of the density gradient fluctuations along the turbulent boundary layer, position the 2P-CFLDI transmit and receive sides on a displacement stage and simultaneously move them in a direction perpendicular to the model wall. Previous single-point CFLDI measurements($\Delta \approx 0.028$ mm) under similar experimental conditions revealed an interesting trend: the amplitude of the density gradient fluctuations increased until $y/\delta \approx 0.8$ and then gradually decreased, stabilizing after $y/\delta \approx 1.5$ [31]. This behavior aligns with findings by Benitez et al. [33,34], who simulated FLDI measurements($\Delta \approx 0.168$ mm) using DNS results ($Ma = 5.86$ and $Re_{\text{unit}} = 1.03 \times 10^7$ m^{-1}).

In Figure 7, the root mean square (rms) of density gradient fluctuations (normalized by using freestream density) is presented along the wall-normal direction at $x = 410$ mm. The wall-normal distance is normalized to the boundary layer thickness measured using Schlieren imaging (see Section 4.1 for specific measurement details). To facilitate a more intuitive comparison of density gradient fluctuations under different experimental conditions, different ranges of axes were used for the vertical coordinate. Figure 7 displays the results obtained for each channel of the current 2P-CFLDI system using black square symbols. The previous CFLDI results [31] are represented by green circle symbols, while the numerical results calculated by Benitez et al. [33,34] are depicted using red triangle symbols. Not surprisingly, the 2P-CFLDI system ($\Delta \approx 0.0715$ mm) yielded consistent results for two optical paths split along the flow direction by a large separation angle Wollaston prism (W_0). The measured density gradient fluctuation intensity followed the expected trend. Notably, as the separation distance Δ increased, the amplitude of density gradient fluctuations also grew, eventually approaching the amplitude of density fluctuations. It is essential to acknowledge that the absolute amplitude difference may arise from the bandwidth of the density fluctuations. At small separation distances Δ, the CFLDI system cannot fully capture the amplitude of large wavelength disturbances, leading to a loss of energy. A similar phenomenon was observed by Parziale [35] when quantifying freestream density fluctuations in a T5 reflective shock tunnel, where corrective measures were applied to refine the measurement results.
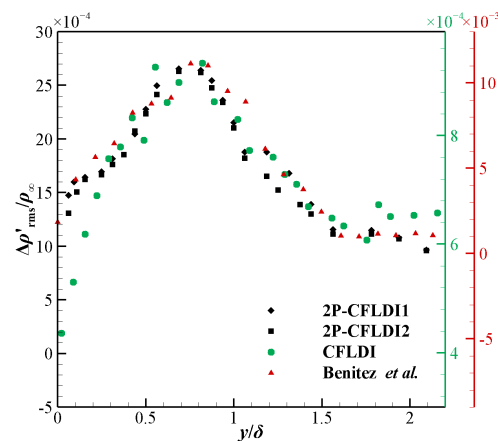

Figure 7. Normalized amplitude profile of density gradient fluctuations as a function of wall-normal distance [33,34].

3.2. Power Spectral Density (PSD)

The PSD is a fundamental measure used to gain insights into the frequency content and behavior of the signal. In this context, Welch's method [36] is employed to estimate PSD. This method enhances frequency resolution and mitigates spectral leakage by segmenting the signal into overlapping windows. Each segment is then analyzed individually, and their periodograms (representing the power at different frequencies) are averaged. The resulting estimate provides a smoother and more accurate representation of the signal's PSD. Mathematically, Welch's method can be expressed as follows:

$$\hat{P}(f_n) = \frac{1}{K}\sum_{k=1}^{K}\frac{L}{U}|A_k(n)|^2, \tag{3}$$

where K denotes the total number of segments, L is the length of each segment, U is the normalization factor, and $A_k(n)$ corresponds to the discrete Fourier transforms of the k-th sequence x_k:

$$A_k(n) = \frac{1}{L}\sum_{j=0}^{L-1} x_k(j)w(j)e^{-2kijn/L}, \tag{4}$$

In this formulation, a Hamming window function (5) is applied to each segment. The input signal is divided into segments of length 2^{16} with 50% overlap.

$$w(j) = \frac{1}{2}\left[1-\cos\left(\frac{2\pi j}{N}\right)\right], \tag{5}$$

To facilitate a comparison of CFLDI measurements with results obtained by other means, emphasis is placed on the normalized PSD. Specifically, by using the rms values, freestream velocity, and boundary layer thickness, the PSD of the integrand over the entire range of transverse coordinates is made equal to exactly 1. This formulation ensures consistency in this study when dealing with frequency domain results.

Figure 8a depicts the normalized power spectral density of density gradient fluctuation measured by using the 2P-CFLDI system near the wall. The measurement results of the two CFLDI channels overlap and match well with the spectral results of the PCB sensor on the wall at the corresponding location. This finding verifies the responsiveness of 2P-CFLDI to disturbances. The 2P-CFLDI system has good channel scalability and precise spatial resolution, making it suitable for inter-correlation analysis, such as convective velocity measurement.

Furthermore, the PSD of the 2P-CFLDI system was compared with the turbulent boundary layer DNS results of Duan et al. [37] under similar conditions ($Ma = 5.86$ and $Re_{unit} = 1.03 \times 10^7$ m^{-1}). The results showed that the measurement spectra of the 2P-CFLDI system are in good agreement with the DNS results, both near the wall and in the freestream. This finding further proves the ability of the 2P-CFLDI system to resolve disturbances. It also verifies that the flow at the measurement location has developed into a fully developed turbulent boundary layer, which is suitable for the development of follow-up studies.
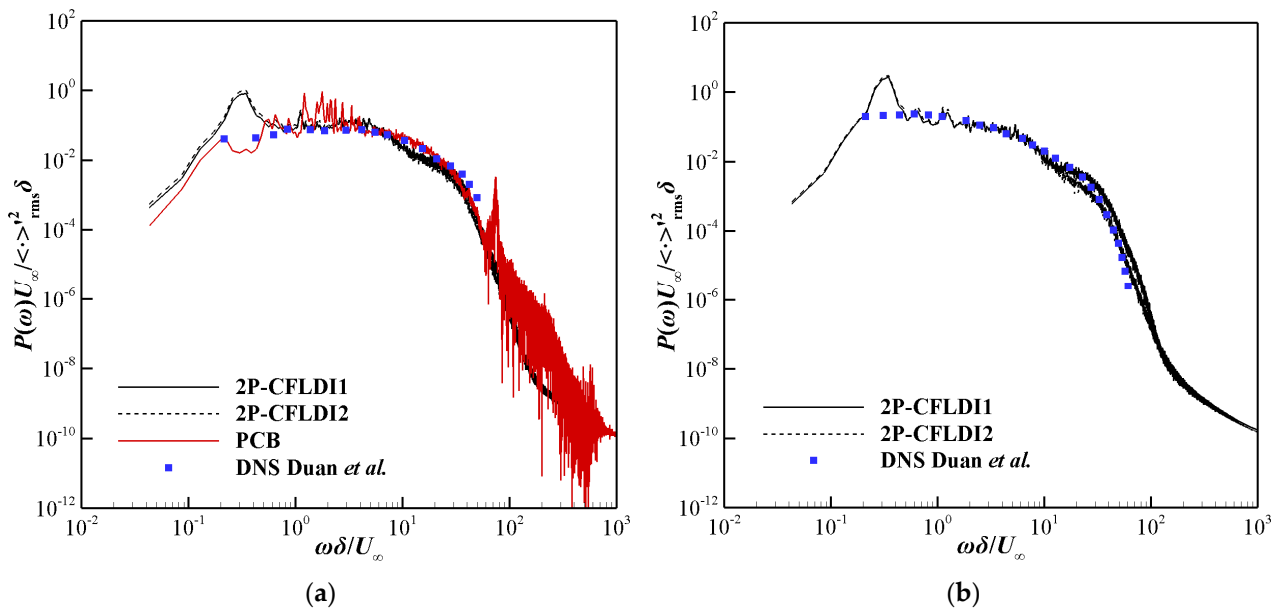
Figure 8. Normalized frequency spectrum of PCB and CFLDI signals at measurement location on the wall. Compared with the DNS result of turbulent boundary layer: (**a**) wall; (**b**) freestream [37].

4. Results

4.1. Schlieren

To visualize the turbulent boundary layer, Schlieren images with a resolution of 576×500 pixels were used to photograph the region near the plate wall. The photograph was taken approximately 530 to 650 mm downstream of the model's leading edge. Before conducting the wind tunnel experiment, the image scale was meticulously calibrated using an optical standard calibration plate with precisely defined graphics. The initial image taken prior to the wind tunnel operation served as the reference. To eliminate background noise, the gray value at the corresponding location in the reference image was subtracted from the gray value of each frame during the experiment. Furthermore, the contrast of all images was enhanced to accentuate the difference between gray values inside and outside the boundary layer. This adjustment facilitated the identification of the boundary layer's edge.

In Figure 9, the processed Schlieren image reveals that the gray value within the boundary layer (appearing close to black) is significantly lower than that of the freestream (appearing close to white). To pinpoint the boundary layer's location, we averaged the gray values across all post-processed images during the steady operation of the wind tunnel. The edge of the boundary layer was determined at the point where the average pixel intensity transitioned from the freestream to the wall, reaching 0.99 times the mean gray value of the freestream. This critical location is denoted by a black horizontal dashed line in Figure 9. The thickness of the boundary layer near the measurement site was determined from the Schlieren image to be approximately 19.5414 mm. This information is crucial for achieving better normalization of the subsequent data.

To better visualize the turbulent boundary layer disturbance noise radiation, the average grey map of all images taken during the steady operation of the wind tunnel is selected as the reference image. The grey value of each frame during the experiment is subtracted from the grey value of the corresponding position in the reference image, which results in a different image that highlights the regions where the noise radiation is stronger or weaker than the background level. In addition, the contrast of all images was likewise enhanced to improve the visibility of the noise features by stretching the range of the grey values. The final obtained image is shown in Figure 10. It depicts the distribution of the radiation angle of the disturbance structure at a certain moment. The noise radiation

angles obtained by Duan et al. through numerical Schlieren [37] and plane–acoustic wave relations [38] are $\mu_1 = 21°$ and $\mu_2 = 30°$, respectively. The Schlieren image obtained in this experiment shows that the far-field noise radiation angle is closer to 21°, and the angle increases at the position close to the boundary layer edge.
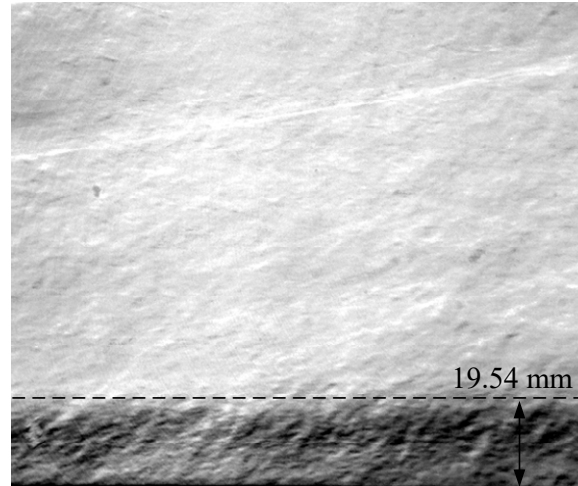

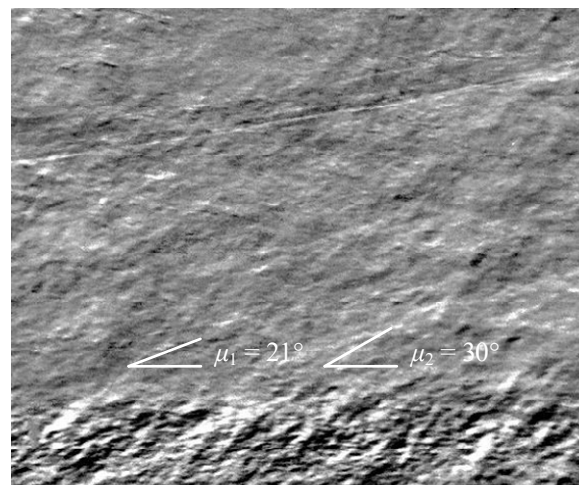**Figure 9.** Post-processed Schlieren image for boundary layer thickness calculation.

Figure 10. Post-processed Schlieren image for disturbance structure visualization.

According to the Mach angle relation [39], the radiation angle of an acoustic wave is related to the relative Mach number between the freestream and the sound source [7]:

$$\sin \mu = \frac{1}{(1 - u_c/u_\infty)Ma}, \tag{6}$$

By measuring the acoustic radiation angle μ, the relative Mach number between the freestream and the sound source can be calculated, and then the convective velocity of the sound source can be determined. Based on Equation (6) and the measurements of the Schlieren above, it can be roughly deduced that the convective velocity of the disturbance structure is about $0.535u_\infty$ outside the boundary layer. The result here is slightly lower than the hot-wire result of Owen and Horstman [13]. This difference may be due to the limitation of the sampling frequency of the Schlieren that prevents the display of high-frequency small-scale disturbance structures. Additionally, the spatial intermittency of the disturbance structures in the measurement region may also contribute to the discrepancy.

4.2. 2P-CFLDI

According to Laufer [40], the convection velocity of density fluctuations can be estimated from space–time correlation results at two neighboring points. The correlation between two signals can be computed using the cross-correlation function, which measures the similarity between two signals as a function of the time lag between them. The cross-correlation function is defined as follows:

$$R_{12}(\tau) = \int_{-\infty}^{\infty} x_1(t)x_2(t - \tau)dt, \tag{7}$$

where $x_1(t)$ and $x_2(t)$ are the two signals, and τ is the time lag. In the current 2P-CFLDI system, the convective velocity is defined as follows:

$$u_c = \Delta x / \Delta t \tag{8}$$

where Δx is the distance between the two focal pairs at the measurement position (here $\Delta x \approx 0.726$ mm), and Δt is the time lag that maximizes the correlation coefficient. Figure 11 shows a plot of the convective velocity u_c along the wall-normal distance measured using the 2P-CFLDI system. The black and red solid lines represent the DNS results for local mean velocity u_l and convective velocity u_c, respectively, from Duan et al. [37]. All velocities are normalized by the freestream velocity. Similar to pressure fluctuations, convective velocities of density fluctuations are significantly larger than local mean velocity near the wall. This area is a major noise source area with high radiant energy. As wall-normal distance increases, convective velocity gradually approaches local mean velocity and remains consistent with it for a certain portion of the boundary layer. Outside the boundary layer ($y/\delta > 1$), convective velocity begins to decrease until it reaches a constant value over $y/\delta \approx 1.5$. This deviation in freestream may be due to stronger evolution effects of density waves outside the boundary layer. Similar phenomena have been observed in incompressible flows [41].
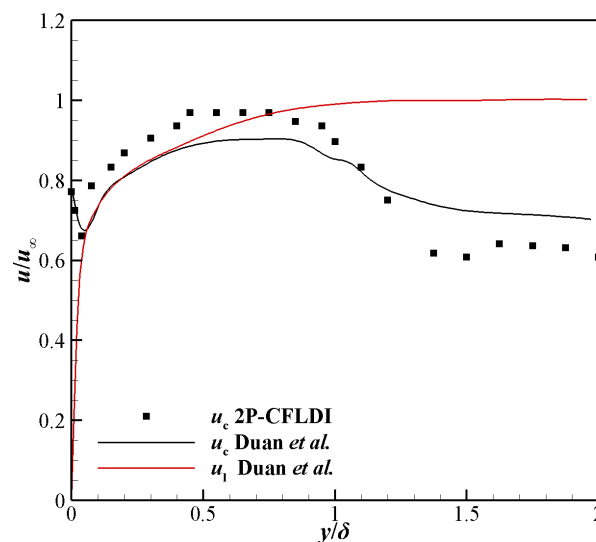

Figure 11. Convection velocities across the hypersonic turbulent boundary layer [37].

Figure 12 compares convective velocities at the wall and in the freestream with some of the available experimental and simulation results. On the wall, the convective velocities measured using 2P-CFLDI are slightly lower than the DNS results from Duan et al. [37] while higher than the trend of the experimental results from Kistler and Chen [42]. This discrepancy may be due to the fact that it was not possible to ensure that the measurement position was completely on the wall during the experiments (there was still some slight distance from the wall). In the freestream, the convective velocity measured using 2P-

CFLDI matches the trend of the experimental data from Laufer [40] but is significantly lower than that of the DNS results from Duan et al. [37]. This discrepancy may be due to the difference in the method used to calculate the convective velocity between the experimental and numerical means. In Figure 12b, $M_r = (u_\infty - u_c)/a_\infty$ (a_∞ denotes the speed of sound in the freestream condition), and the area below the black solid line $M_r = 1$ (i.e., the area where $M_r > 1$) is associated with supersonic convective disturbance relative to the freestream. The convective velocities measured in this study are within this region, indicating that the disturbance structure convects supersonically to the freestream and generates noise radiation. This phenomenon is consistent with the concept of "Eddy Mach wave radiation" in supersonic flows. The ability of 2P-CFLDI to measure convective velocities is further validated.
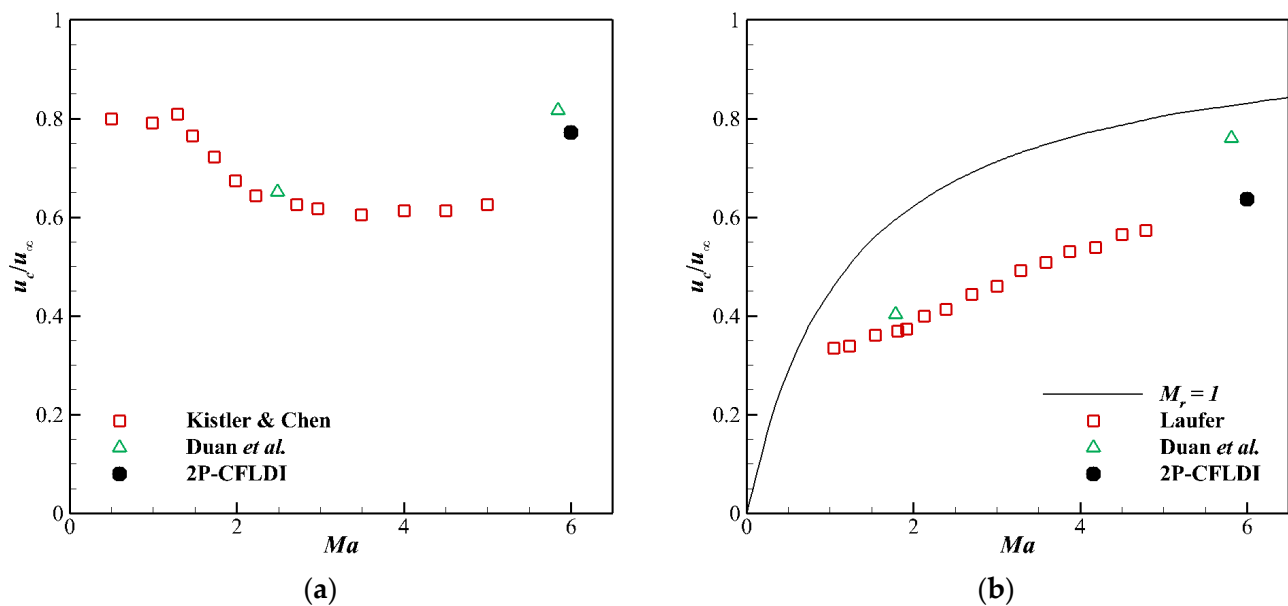

Figure 12. Comparison of convective velocity under different freestream Mach number: (**a**) wall; (**b**) freestream [37].

After the raw data are processed using band-pass filtering, convective velocities for different scales of density fluctuation waves can be obtained by using the same method as above. Figure 13 illustrates the change in convective velocity along the boundary layer for different bandwidths of disturbances. Within the boundary layer, density fluctuations of different scales are approximately convecting at the local mean convective velocity. As the position moves into the free stream, large-scale disturbances still convect at the local mean convective velocity, while the convective velocity of small-scale disturbances increases significantly. The smaller the scale, the closer the convective velocity approaches the local mean velocity. This variation of convective velocity with density fluctuation scales is consistent with Owen's measurements using a hot wire in hypersonic flows [13]. These observations suggest that the convective velocities of the disturbances are mainly determined by the large-scale disturbances because the energy of the small-scale disturbances is weaker and dissipates faster. Consequently, the large-scale disturbances near the wall are considered to be the primary source of noise radiation for the hypersonic turbulent boundary layer.
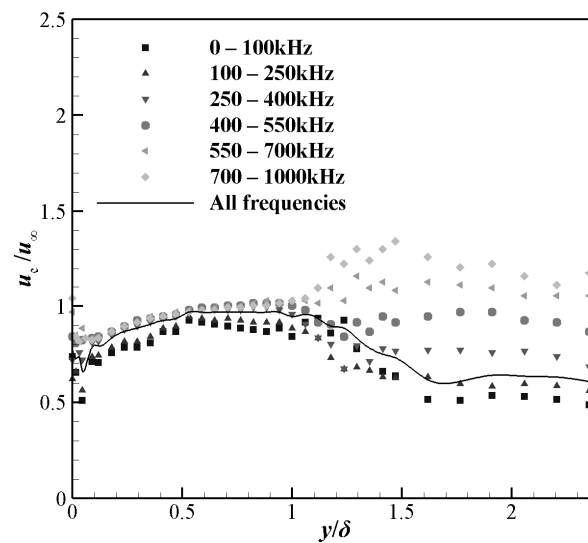
Figure 13. Comparison of convective velocity profiles under different bandpass filtering across the hypersonic turbulent boundary layer.

5. Conclusions

A modified 2P-CFLDI system was employed to measure the density fluctuations arising from a turbulent boundary layer with zero pressure gradient ($Ma = 6$, $Re = 1 \times 10^7$ m^{-1}). The system was used to study the variation in the convective velocity of the disturbances at different scales along the wall-normal direction. The disturbance structure in the measurement region was visualized using a Schlieren system. The 2P-CFLDI system's ability to measure convective velocities in hypersonic flow was experimentally verified, leading to a better understanding of the causes of noise radiation from the hypersonic turbulent boundary layer.

The use of image post-processing methods allows for the acquisition of more visualized images of disturbances in the measurement region. However, due to the limitation of the sampling frequency, the Schlieren mainly reflects the transient structure of large-scale disturbances. The convective velocity of the disturbances is faster than the local mean velocity near the wall, and the turbulent structure in this region is more energetic and coherent, producing stronger noise radiation. The convective velocity of large-scale disturbances tends to be smaller than that of small-scale disturbances. The difference between the convective velocity of the fluctuating structure and the local mean convective velocity increases with distance from the wall and becomes more pronounced as the scale of the disturbance increases. The scaling effect is significantly stronger outside of the boundary layer than that of the inside. The convective velocity of the disturbances is mainly determined by the large-scale disturbances, as small-scale disturbances exhibit weaker energy and faster dissipation. Therefore, it is hypothesized that large-scale disturbances near the wall are the primary source of noise radiation from the hypersonic turbulent boundary layer.

The results obtained by the 2P-CFLDI system follow the trend of previous experimental and numerical results, which are consistent with the theory of Eddy Mach wave radiation. This verification of the accuracy and reliability of the measurement technique is significant. The 2P-CFLDI system has the advantage of being able to measure the convective velocities of density fluctuations inside and outside the boundary layer without any interference or error from the sensor size. Overall, these observations can be used to understand the principles of radiated noise in the turbulent boundary layer, as well as to validate and improve the numerical models and the theoretical predictions of eddy Mach wave radiation. However, the current study also faces some limitations and challenges, such as the difficulty of ensuring the measurement position on the wall, the difference in the calculation of the convective velocity between the experimental and the numerical methods,

and the influence of tunnel turbulent boundary layer on the experimental results. These issues need to be addressed and resolved in future studies.

References

1. Bertin, J.J. *Hypersonic Aerothermodynamics*; AIAA Education Series; American Institute of Aeronautics and Astronautics: Washington, DC, USA, 1994; ISBN 978-1-56347-036-3.
2. Beckwith, I.E. Development of a High Reynolds Number Quiet Tunnel for Transition Research. *AIAA J.* **1975**, *13*, 300–306. [CrossRef]
3. Laufer, J. Some Statistical Properties of the Pressure Field Radiated by a Turbulent Boundary Layer. *Phys. Fluids* **1964**, *7*, 1191. [CrossRef]
4. Schneider, S.P. Development of Hypersonic Quiet Tunnels. *J. Spacecr. Rocket.* **2008**, *45*, 641–664. [CrossRef]
5. Phillips, O.M. On the Generation of Sound by Supersonic Turbulent Shear Layers. *J. Fluid. Mech.* **1960**, *9*, 1–28. [CrossRef]
6. Ffowcs Williams, J.E. The Noise from Turbulence Convected at High Speed. *Philos. Trans. R. Soc. London Ser. A Math. Phys. Sci.* **1963**, *255*, 469–503. [CrossRef]
7. Laufer, J. Aerodynamic Noise in Supersonic Wind Tunnels. *J. Aerosp. Sci.* **1961**, *28*, 685–692. [CrossRef]
8. Kaimal, J.C.; Wyngaard, J.C.; Izumi, Y.; Coté, O.R. Spectral Characteristics of Surface-layer Turbulence. *Q. J. R. Meteorol. Soc.* **1972**, *98*, 563–589. [CrossRef]
9. Willmarth, W.W.; Wooldridge, C.E. Measurements of the Fluctuating Pressure at the Wall beneath a Thick Turbulent Boundary Layer. *J. Fluid. Mech.* **1962**, *14*, 187–210. [CrossRef]
10. Schewe, G. On the Structure and Resolution of Wall-Pressure Fluctuations Associated with Turbulent Boundary-Layer Flow. *J. Fluid. Mech.* **1983**, *134*, 311–328. [CrossRef]
11. Bull, M.K. Wall-Pressure Fluctuations beneath Turbulent Boundary Layers: Some Reflections on Forty Years of Research. *J. Sound. Vib.* **1996**, *190*, 299–315. [CrossRef]
12. Klinner, J.; Hergt, A.; Willert, C. Experimental Investigation of the Transonic Flow around the Leading Edge of an Eroded Fan Airfoil. *Exp. Fluids* **2014**, *55*, 1800. [CrossRef]
13. Owen, F.K.; Horstman, C.C. On the Structure of Hypersonic Turbulent Boundary Layers. *J. Fluid. Mech.* **1972**, *53*, 611–636. [CrossRef]
14. Spina, E.F.; Donovan, J.F.; Smits, A.J. Convection Velocity in Supersonic Turbulent Boundary Layers. *Phys. Fluids A Fluid. Dyn.* **1991**, *3*, 3124–3126. [CrossRef]
15. Krogstad, P.A.; Kaspersen, J.H.; Rimestad, S. Convection Velocities in a Turbulent Boundary Layer. *Phys. Fluids* **1998**, *10*, 949–957. [CrossRef]
16. Russo, G.P. Hot Wire Anemometer. In *Aerodynamic Measurements*; Elsevier: Amsterdam, The Netherlands, 2011; pp. 67–98. ISBN 978-1-84569-992-5.
17. Finke, C.P. Temperature-Compensated Calibration and Measurements with Cross-Style Hotwire Anemometers. Master's Thesis, Texas A&M University, College Station, TX, USA, 2021.
18. Siddiqui, F.; Gragston, M.; Bowersox, R.D.W. Measurement of Wall-Cooling Effects on Hypersonic Boundary-Layer Transition Using Focused Laser Differential Interferometry. *AIAA J.* **2022**, *60*, 6214–6224. [CrossRef]
19. Li, H.; Li, Y.; Chen, L.; Yao, X. Tunable Spatial Resolution Focused Laser Differential Interferometer for Density Fluctuation Measurement. *Appl. Sci.* **2023**, *13*, 3253. [CrossRef]
20. Camillo, G.P.; Wagner, A.; Toki, T.; Scalo, C. Combined Experimental and Numerical Investigation of a Hypersonic Turbulent Boundary Layer by Means of FLDI and Large-Eddy Simulations. *Aerospace* **2023**, *10*, 570. [CrossRef]
21. Houpt, A.; Leonov, S. Cylindrical Focused Laser Differential Interferometer. *AIAA J.* **2021**, *59*, 1142–1150. [CrossRef]
22. Hopkins, K.J.; Porat, H.; McIntyre, T.J.; Wheatley, V.; Veeraragavan, A. Measurements and Analysis of Hypersonic Tripped Boundary Layer Turbulence. *Exp. Fluids* **2021**, *62*, 164. [CrossRef]

23. Jewell, J.S.; Parziale, N.J.; Lam, K.-L.; Hagen, B.J.; Kimmel, R.L. Disturbance and Phase Speed Measurements for Shock Tubes and Hypersonic Boundary-Layer Instability. In Proceedings of the 32nd AIAA Aerodynamic Measurement Technology and Ground Testing Conference, Washington, DC, USA, 13–17 June 2016; AIAA AVIATION Forum. American Institute of Aeronautics and Astronautics: Orlando, FL, USA, 2016.

24. Gillespie, G.I.; Ceruzzi, A.P.; Laurence, S.J. A Multi-Point Focused Laser Differential Interferometer for Characterizing Freestream Disturbances in Hypersonic Wind Tunnels. *Exp. Fluids* **2022**, *63*, 180. [CrossRef]

25. Hildebrand, N.; Choudhari, M.M.; Deegan, C.P.; Huang, J.; Duan, L. Direct Numerical Simulation of Acoustic Disturbances in a Hypersonic Two-Dimensional Nozzle Configuration. *AIAA J.* **2022**, *60*, 3452–3463. [CrossRef]

26. Auvity, B.; Etz, M.R.; Smits, A.J. Effects of Transverse Helium Injection on Hypersonic Boundary Layers. *Phys. Fluids* **2001**, *13*, 3025–3032. [CrossRef]

27. Williams, O.J.H.; Smits, A.J. Effect of Tripping on Hypersonic Turbulent Boundary-Layer Statistics. *AIAA J.* **2017**, *55*, 3051–3058. [CrossRef]

28. Weisberger, J.M.; Bathel, B.F.; Herring, G.C.; Buck, G.M.; Jones, S.B.; Cavone, A.A. Multi-Point Line Focused Laser Differential Interferometer for High-Speed Flow Fluctuation Measurements. *Appl. Opt.* **2020**, *59*, 11180. [CrossRef]

29. Ceruzzi, A.; Callis, B.; Weber, D.; Cadou, C.P. Application of Focused Laser Differential Interferometry (FLDI) in a Supersonic Boundary Layer. In *AIAA Scitech 2020 Forum*; AIAA SciTech Forum; American Institute of Aeronautics and Astronautics: Orlando, FL, USA, 2020.

30. Ceruzzi, A.; McManamen, B.; Cadou, C.P. Demonstration of Two-Point Focused Laser Differential Interferometry (2pFLDI) in a Mach 18 Flow. In *AIAA Scitech 2021 Forum*; AIAA SciTech Forum; American Institute of Aeronautics and Astronautics: Orlando, FL, USA, 2021; 2p.

31. Huang, R.; Liu, W.; Cheng, J.; Wu, J. Measurement of Hypersonic Turbulent Boundary Layer on a Flat Plate Using Cylindrical Focused Laser Differential Interferometer. *Phys. Fluids* **2023**, *35*, 035121. [CrossRef]

32. Parziale, N. Slender-Body Hypervelocity Boundary-Layer Instability. Ph.D. Thesis, California Institute of Technology, Pasadena, CA, USA, 2013.

33. Benitez, E.K.; Borg, M.P.; Luke Hill, J.; Aultman, M.T.; Duan, L.; Running, C.L.; Jewell, J.S. Quantitative Focused Laser Differential InterferomXetry with Hypersonic Turbulent Boundary Layers. *Appl. Opt.* **2022**, *61*, 9203–9216. [CrossRef]

34. Benitez, E.K.; Borg, M.P.; Rhodes, C.; Jewell, J.S. Optical-Axis Spatial Sensitivity of a Simulated Focused Laser Differential Interferometer. *AIAA J.* **2023**, *61*, 1925–1938. [CrossRef]

35. Parziale, N.J.; Shepherd, J.E.; Hornung, H.G. Free-Stream Density Perturbations in a Reflected-Shock Tunnel. *Exp. Fluids* **2014**, *55*, 1665. [CrossRef]

36. Welch, P. The Use of Fast Fourier Transform for the Estimation of Power Spectra: A Method Based on Time Averaging over Short, Modified Periodograms. *IEEE Trans. Audio Electroacoust.* **1967**, *15*, 70–73. [CrossRef]

37. Duan, L.; Choudhari, M.M.; Zhang, C. Pressure Fluctuations Induced by a Hypersonic Turbulent Boundary Layer. *J. Fluid Mech.* **2016**, *804*, 578–607. [CrossRef] [PubMed]

38. Liepmann, H.W.; Roshko, A. *Elements of Gasdynamics*; Courier Dover Publications: Westford, MA, USA, 1957; ISBN 0-486-41963-0.

39. Sasoh, A. *Compressible Fluid Dynamics and Shock Waves*; Springer: Singapore, 2020; ISBN 9789811505034.

40. Laufer, J. *Sound Radiation from a Turbulent Boundary Layer*; Jet Propulsion Lab: Pasadena, CA, USA, 1964; JPL-TR-32-119.

41. Kim, J.; Hussain, F. Propagation Velocity of Perturbations in Turbulent Channel Flow. *Phys. Fluids A Fluid Dyn.* **1993**, *5*, 695–706. [CrossRef]

42. Kistler, A.L.; Chen, W.S. The Fluctuating Pressure Field in a Supersonic Turbulent Boundary Layer. *J. Fluid Mech.* **1963**, *16*, 41–64. [CrossRef]